IEEE Sensors Council

Sensorization of Soft Robot Joints for Accurate and Durable Bending Measurement

Elia Landi, *Member, IEEE*, Tommaso Lisini Baldi, *Member, IEEE*, Jonas Papenbrock, *Student Member, IEEE*, Alessio Facello, *Member, IEEE*, Andrea Prato, *Member, IEEE*, Alessandro Schiavi, *Member, IEEE*, Marco Mugnaini, *Member, IEEE*, Domenico Prattichizzo, *Fellow, IEEE*, and Ada Fort, *Member, IEEE*

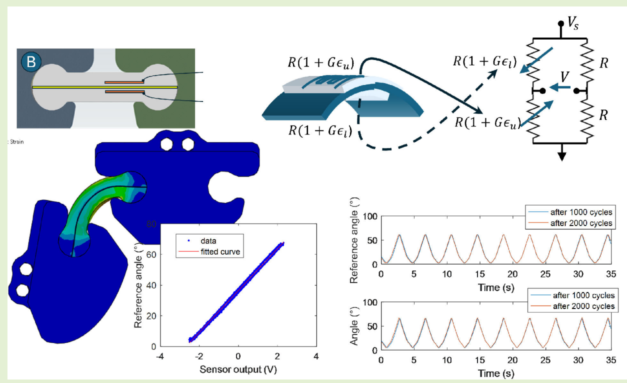

***Abstract*—In the practical implementation of soft robots, accurately tracking the deformation of links (or joints) is crucial for obtaining proper control. Therefore, there is a need for lightweight, durable, and cost-effective solutions to monitor the movement of soft segments. This study proposes sensor-equipped flexible joints capable of measuring the angle between the segments of a robotic finger, considering pure in-plane bending. Initially, these joints were simulated to assess their mechanical behavior and the feasibility of accommodating strain gauges to measure differential strain, which correlates with angle measurements. Based on the simulation results, three types of sensor-equipped joints with distinct mechanical properties were developed. These joints were characterized in terms of angle measurement accuracy and durability. The experimental evaluation assessed that maximum error, compared to an accurate reference angle measured using a MEMS accelerometer, was less than 1.5°. Durability tests demonstrated that joint performance remained stable over more than 3500 bending cycles, during which the joints were bent up to approximately 65°; the measured angle drift remained below 2°.**

***Index Terms*—Human–robot interaction, sensors, soft robots.**

I. Introduction

SOFT robots exhibit distinctive characteristics when compared to their rigid counterparts, since they employ hyperelastic materials, including polymers, rubber, silicone, and other flexible components [1], [2], [3], [4].

Received 26 December 2024; revised 7 March 2025; accepted 10 March 2025. Date of publication 27 March 2025; date of current version 15 May 2025. This work was supported by the Italian Ministry of Research, under the complementary actions to the NRRP “Fit4MedRob-Fit for Medical Robotics” under Grant PNC0000007 (CUP B53C22006930001). The associate editor coordinating the review of this article and approving it for publication was Prof. Mohsen Asadnia.

(Corresponding author: Elia Landi.)

Elia Landi, Jonas Papenbrock, Marco Mugnaini, and Ada Fort are with the Department of Information Engineering and Mathematics, University of Siena, 53100 Siena, Italy (e-mail: elia.landi@unisi.it; jonas.papenbrock@unisi.it; marco.mugnaini@unisi.it; ada.fort@unisi.it).

Tommaso Lisini Baldi and Domenico Prattichizzo are with the Department of Information Engineering and Mathematics, University of Siena, 53100 Siena, Italy, and also with the Department of Humanoids and Human Centered Mechatronics, Istituto Italiano di Tecnologia, 16163 Genoa, Italy (e-mail: tommaso.lisini@iit.it; domenico.prattichizzo@iit.it).

Alessio Facello, Andrea Prato, and Alessandro Schiavi are with the Division of Applied Metrology and Engineering, National Institute of Metrological Research (INRiM), 10135 Turin, Italy (e-mail: a.facello@inrim.it; a.prato@inrim.it; a.schiavi@inrim.it).

Digital Object Identifier 10.1109/JSEN.2025.3552897

Moreover, softness offers several advantages, including intrinsic safety and exceptional versatility, making robots capable of performing a wide range of tasks. For example, in human–robot interaction, soft robots can safely collaborate with humans. In delicate object manipulation, they can handle fragile objects without causing damage. Particularly, in assistive and rehabilitation scenarios, soft robots can be used for tasks like providing physical support or aiding in movement therapy.

The integration of proprioceptive and tactile sensing can greatly enhance soft robot abilities to sense and respond to various physical factors. However, fully equipped devices are still limited and there is significant room for improvement. For instance, soft robots can be significantly enriched by incorporating proprioceptive and tactile sensing capabilities, encompassing measurements of strain, pressure, bending, twisting, and other physical parameters [5]. Even if multiple technologies have been proposed in research [6], [7], [8], there is still significant ongoing research aimed at improving performance, especially in terms of accuracy and stability. With specific regard to proprioceptive sensors, specifically aiming at measuring the curvature of robot components,

(a) (b)

Fig. 1. Representative use case of using the RSF. (a) User wearing an RSF. (b) Detailed view of the finger used for grasping a bottle of water.

those proposed in the literature are usually based on "soft technologies" including low modulus (less than 1 MPa) elastomers with liquid-phase material filled channels and resistive, capacitive, or inductive reading [9] stretchable conductive materials, elastomeric conductors, which consist of elastomers loaded with conductive micro/nano particles/wires, such as silver nanowires, silver particles, carbon nanotubes, and graphene, piezoelectric polymers, and so on [10]. Unfortunately, these sensing technologies have a limited lifespan and poor reliability.

Despite the common assertion that the deformable nature of soft robots or wearable robot components limits the use of conventional sensors (e.g., encoders, strain gauges, etc.) [11], accurate designs and the use of multiple materials or composites can adapt some of these established technologies to provide accurate and reliable measurements for some specific applications [12], [13].

In this work, we focused on a silicone soft joint specifically designed to enable bending in robotic fingers, used here as a representative case. The joint studied is part of an additional robotic finger, known as the robotic sixth finger (RSF), which aims to restore grasping abilities in patients with limited hand mobility due to paralysis or other motor impairments [14], [15]. The RSF utilizes the same mechanical principles as other soft hands and grippers like the devices proposed in [16]. In Fig. 1, a user wearing the RSF and using it for grasping an object is depicted. On the one hand, soft robotic grippers offer several advantages over the rigid ones, making them particularly suitable for various applications. Key benefits include adaptability to the objects shape, intrinsic safety, enhanced gripping capabilities, durability, and ease of use in human–robot collaboration [17], [18], [19]. On the other hand, deformable materials are challenging to model accurately and predicting trajectories and link displacements a priori in human–robot collaboration scenarios is difficult. Effectively measuring intermodule forces and displacements to optimize grasp performance remains an open topic.

With this work, we present the development, characterization, and validation of flexible sensors for soft-robot joints obtained by embedding metal thin-film or foil strain gauges within the joints to measure their bending angle. The procedure here described was tested on a soft joint exploited in multiple soft robots (e.g., the RSF (shown in Fig. 1) [15], [20] and grippers [21], [22]) but can be easily extended to all the silicone-based soft joints.

II. State of the Art and Statement of the Problem

Soft joints inherently allow for bending and a wide range of other deformations. This versatility is both an advantage and a limitation. While it enhances the adaptability of soft robots, it complicates precise control. In the context of applications, such as manipulators or the "sixth finger" for grasping tasks, the primary requirement is to limit joint movement to achieve pure bending. This could be achieved by designing specialized structures that encourage such constrained motion [23], [24].

In general, accurately sensing the state of a soft joint deforming freely is nearly impossible without implementing multiaxis or multimode sensing systems. However, these solutions bring substantial challenges in terms of connection complexity and integration. Therefore, in our case, we focus on measuring only 1-D bending, where the joint follows a controlled planar trajectory. This approach reduces the complexity and enhances reliability, providing a practical proprioceptive solution within the application of interest. The straightforward approach for measuring bending focuses on integrating flexible strain sensors [25], [26], which must adapt to joint functions. Strain sensors for soft components are often based on structures capable of withstand very large deformation, such, for instance, those that incorporate flexible microchannels filled with conductive fluids, where deformation changes the cross-sectional area, modifying electrical resistance and enabling precise strain measurements [27].

Another method involves using biocompatible solutions, such as sodium chloride, within soft channels to measure stretching while remaining safe for applications in contact with biological environments [28].

While these methods provide high customization and can be tailored to various soft robotic shapes, they often come with complex manufacturing requirements that impact sensor durability and performance stability.

Optical fibers represent another promising route for measuring deformation, as shown in studies where they capture bending, elongation, and compression within soft modules [29]. The fiber Bragg grating (FBG) technology, for instance, offers highly accurate measurements of force and shape [30]. However, the specialized equipment needed to interpret FBG data can be prohibitively expensive and complicated integration into modular systems. Hall-effect sensors, which sense proximity to magnetic sources, also offer noncontact measurements of curvature with high precision, but they are sensitive to interference from nearby electromagnetic fields, limiting their use in certain environments [31].

As an alternative, resistive metal strain sensors provide a cost-effective and compact solution. Among these, the so-called "flex" sensors, also available as commercial solutions, have often been proposed for soft robotics [32], [33], [34]. Commonly used in wearable devices, these sensors rely on flexible substrates coated with conductive ink withstanding very large deformations. Bending the sensor stretches the ink layer, which causes conductive particles to move and modify the resistance. In these sensors, it is primarily the substrate that deforms, while the internal structure of the conductive materials responds nonlinearly to the deformation. This change in resistance, directly related to the bending, allows for measuring one-directional curvatures without compromising flexibility [32]. However, these sensors suffer from signal drift over time and limited performance in dynamic conditions [32]. They have often a nonlinear and low sensitivity at small angles (below 30° or 45°) [32], [33], [34], which is problematic for applications, such as robotic joints of the sixth finger for grasping purpose, where small angles dominate. In any case, the issue of coupling the resistive sensor with the soft joint is an open problem, whose solution is often related to the specific application. Ensuring proper adhesion without introducing creep and securing effective mechanical coupling remains a challenge, as does guaranteeing stable and durable electrical contacts.

The solution proposed in this article is similar to other approaches based on embedded flex sensors [34]. Our approach differs by employing traditional metal strain gauges based on thin-film or foil technology produced through precise thin-film deposition or etching techniques. In these sensors, the metal layer has an ordered and controlled microstructure, which gives the sensor predictable and repeatable behavior, allowing for precise strain measurements designed to work in the linear elastic regime, meaning they can measure small deformations, typically up to 1%–2% strain. Notwithstanding these measurement range limitations, positioning them near the neutral axis of the bending joint mitigates the issue, enabling them to operate effectively within the small deformation range. As a result, the sensing structure achieves a stable, precise linear response. Additionally, our proposed solution addresses the challenge of ensuring a stable mechanical coupling with the silicone joint, and specific sensor positioning enhances the durability of the electrical contacts.

III. Joint Characterization

In the development of flexible joints for soft robot applications, hyperelastic materials [1], [2], [3], [4], such as silicone, are commonly used. For realizing sensor-equipped flexible joints, the goal is to embed thin-film or foil strain gauges within the joints to measure their curvature. A simulation study was conducted to evaluate the strain distribution across the deformed joint, focusing on how the embedded strain gauges respond to bending. The objective of this study was to simulate the deformation behavior of the embedded sensors under conditions that closely replicate real-world applications. In this context, a preliminary analysis of mechanical properties and elastic/viscoelastic behavior of materials used in the joints is crucial to accurately predict the performance of the strain sensors and ensure the proper functioning of the joints once they are constructed.

A. Material Characterization

In this article, the Mooney–Rivlin model was used for simulating hyperelastic material behavior due to its versatility and accurate predictions for various materials, including rubber and polymers, in very different loading conditions [35], [36], [37], [38]. The generalized Mooney–Rivlin model relates the strain energy density function to a linear combination of invariants of the deformation tensor and J, the determinant of the strain gradient tensor by expressing the strain energy density function W as a linear function of the first and the second invariants $\underline{I}_1, \underline{I}_2$ of $\underline{B} = (\det B)^{-1/3} B$, which is the unimodular component of the Cauchy–Green deformation tensor

$$W = \sum_{p,q=0}^{N} C_{pq} \left(\underline{I}_1 - 3\right)^p \left(\underline{I}_2 - 3\right)^q + \sum_{m=1}^{M} \frac{1}{D_m} (J - 1)^{2m} \quad (1)$$

where C_{pq} are constants related to the distortional deformations and D_m are the material constants related to the volumetric deformations.

Since silicone rubber can be considered incompressible, the last term in (1) can be neglected, and the first-order terms are sufficient to describe the behavior.

Hence, (1) simplifies to

$$W = C_{10}\left(\underline{I}_1 - 3\right) + C_{01}\left(\underline{I}_2 - 3\right). \quad (2)$$

In the case of uniaxial stress, the deformation is characterized by a principal stretch ratio (λ). The other two principal stretch ratios are equal to $(1/\sqrt{\lambda})$ due to the incompressibility constraint.

As a result, the strain energy function is

$$W = C_{10}\left(\lambda^2 + \frac{2}{\lambda} - 3\right) + C_{01}\left(\frac{1}{\lambda^2} + 2\lambda - 3\right). \quad (3)$$

Therefore, for uniaxial tension, the stress σ can be related to the stretch ratio as follows:

$$\sigma = 2\left(\lambda - \frac{1}{\lambda^2}\right)\left(C_{10} + \frac{C_{01}}{\lambda}\right). \quad (4)$$

Equation (4) represents the uniaxial Mooney–Rivlin model, which predicts the material stress–strain behavior under uniaxial loading using only two constants.

These constants can be determined through simple experiments, such as uniaxial tensile tests. The silicone-based material used for fabricating the joints considered in this study (Silicone R-PRO Fast, Reschimica, Italy) was tested to determine the model parameters by conducting Shore A hardness test and compression tests on cylindrical samples with a diameter of 36 mm and a height of 10 mm. The measurements of elastic and viscoelastic properties of the material are carried out with a proper equipment designed to perform accurate characterization of viscoelastic and viscoplastic polymeric soft material, with 0.1 μm of resolution on displacement, and 5 mN of resolution of force, as detailed in [39] and [40]. The test was performed up to 50% of uniaxial compressive deformation (reaching a maximum stress of 2 MPa). Moreover, a series of 60 cycles of hysteresis loop, up to 45% of deformation, confirm the stability of the elastic response, without evident stress losses. The test speed, defined as the rate of material deformation over time, was selected to align with the operating conditions of the joints (0.21 mm/s, a strain rate of $2.1\cdot10^{-1}$ s^{-1}). The material showed typical behavior of a neo-Hookean solid and the (apparent) Young's modulus of the material, increasing as a function of the strain range, can be

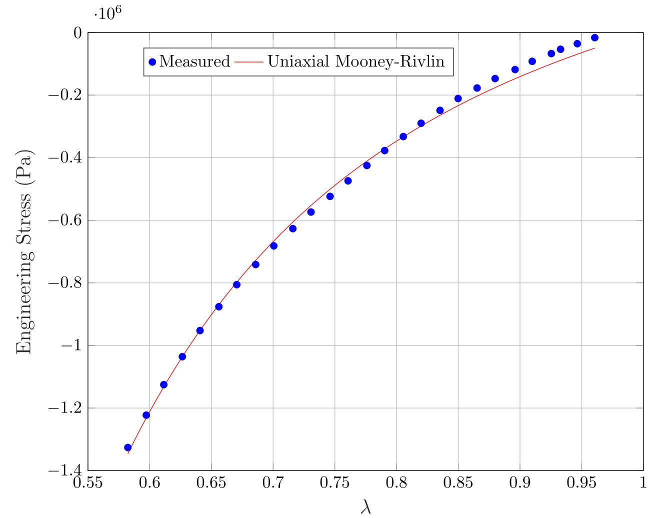

Fig. 2. Engineering stress over strain; blue dots: measured values; red line: uniaxial Mooney–Rivlin model fitting.

treated in terms of "differential modulus," i.e., as $\partial E/\partial \varepsilon$ [41]. According to the value of Shore A hardness test [42], namely $\mathrm{Sh}_A = 34$, the corresponding Young's modulus of the tested material can be derived, yielding $E = 3.6$ MPa [43]. This value is compatible with the experimental (apparent) Young's modulus, determined in compression, within the strain range between 0.3 and 0.4. Finally, experimental data show that, once a static deformation of 50% is imposed, the stress rapidly decreases in the first 30 s (namely, from 2 to 1.8 MPa, i.e., $\sim$10%), while a very slow stress loss occurs over long term. In particular, by fitting the stress relaxation with the KWW function, the calculated relaxation time is $\tau_0 = 2.5{\cdot}10^{10}$ s, with the stretching exponent $\beta = 0.13$ in accordance with [44] and [45].

This evidence allows guaranteeing the ability of the material to keep the stored elastic energy for very long time (without relevant losses) when subjected to large deformation. Once confirmed the hyperelastic behavior of the used silicone-based material, the experimental data of stress–strain test were fitted with the uniaxial Mooney–Rivlin model defined in (4); thereby, the model parameters C_{01} and C_{10} were retrieved.

Fig. 2 reports the least square fitting result (red line) compared with the measurement results (blue dots). The overall fitting root mean square error is lower than 2%.

To accurately determine the optimal sensor placement within the soft joint, simulations were conducted on a typical joint geometry, as shown in Fig. 3(a), where the joint has a dog-bone shape with two ends designed for connecting to the rigid parts. The joint has a width of 20 mm, a length of 17 mm, and a thickness of 3 mm in the center region.

Additionally, the simulation study considered the configuration used for experimental tests [shown in Fig. 3(b)], which consists of two rigid parts (i.e., the phalanxes) and the joint. One of the rigid parts is fixed horizontally, while a vertical force is applied to the opposite end of the other rigid part simulating a scenario where the force is transmitted through a cord or tendon. The magnitude of the applied force was chosen based on the typical force exerted by the motor used

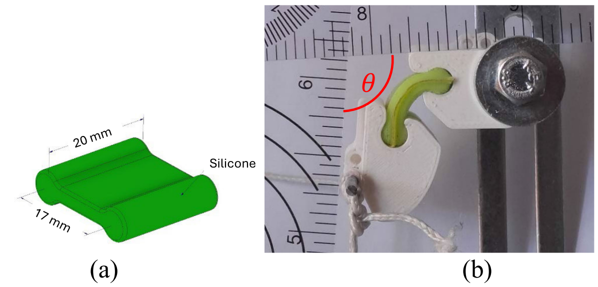

Fig. 3. Design and prototype of an SJ. (a) Design of the joint geometry. (b) SJ during the evaluation process.

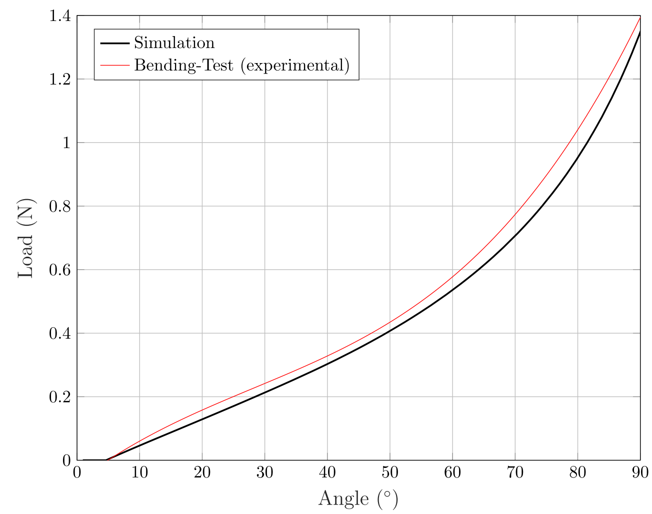

Fig. 4. Behavior of the bending angle with respect to the applied force. Comparison between real behavior and simulated one.

in real applications, such as in a prototype of a sixth finger, specifically in the range 0–1.4 N.

As already mentioned, the objective of these simulations was to identify the most suitable location for the strain gauge sensors, ensuring they are both protected from potential damage due to excessive strain and that the measurement sensitivity is maximized.

Fig. 4 confirms that the proposed model accurately describes the structural behavior, as derived previously. The experimental results exhibit strong agreement with the simulated data, particularly in capturing the relationship between the applied force and joint bending.

The deformation within the joint under the maximum considered load was evaluated and is shown in Fig. 5, which presents the equivalent elastic strain distribution in the bare silicone joint with an applied force of 1.4 N. From the simulations, it can be observed that in the middle region of the joint, up to a thickness of about 300 μm, the strain is approximately a few percentages, whereas the strain at the surface of the joint exceeds 30%. Part of the strain results from the stretching of the joint and part from its bending, meaning that even the middle surface is not neutral and becomes elongated due to the applied load.

This strain component is not relevant to measuring the bending angle, nor to the operation of the joint, as in pure bending the middle surface remains undeformed.

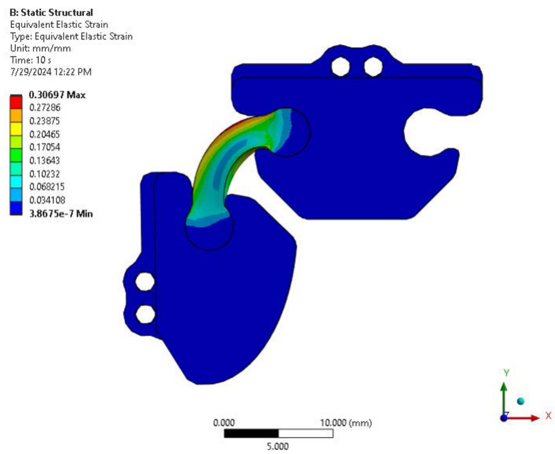

Fig. 5. Equivalent elastic strain distribution in the bare silicone joint.

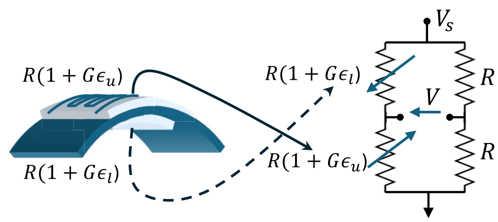

Fig. 6. Strain gauges mounting on the substrate and bridge configuration.

From this evaluation, it can be concluded that using thin-film or foil metal strain gauges, which can only withstand a maximum strain of 2%, could be problematic, even if they are embedded near the middle surface of the joint.

IV. Sensor-Equipped Joint Design

The issue highlighted in Section III, where the middle surface of the joint becomes elongated during bending, can be addressed by embedding a layered structure with metal thin-film or foil strain gauges. This solution has a twofold purpose: reducing joint elongation during bending and providing support for thin-film strain gauges on polymeric substrates. The structure consists of a thin, flexible yet rigid substrate, onto which two metal strain gauges are bonded—one on each side—enabling the formation of Wheatstone bridge configuration. Positioned along the middle surface, where deformation is minimized, the substrate spans the length of the joint, supporting the strain gauges and limits elongation under mechanical loads by modifying the joint overall behavior.

In other words, the layered structure employs a classical approach for measuring bending, featuring two strain gauges adhered to the top and bottom surfaces of the substrate, configured in a half-bridge arrangement. As shown in Fig. 6, these strain gauges are positioned at equal distances from the middle surface on opposite sides. This setup enables accurate bending measurement while minimizing the effects of residual stretching, compression, and torsion and effectively rejecting common-mode effects.

Using this configuration, with the bridge completed with two resistors with the same resistance R as the strain gauges,

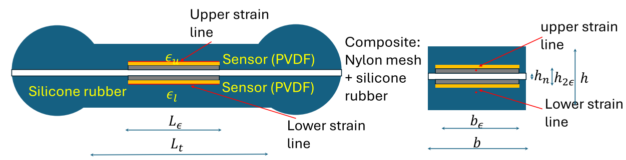

Fig. 7. Sensors positioning within the joint.

the sensing structure output is a voltage V_0 proportional to the differential strain and related to the bending angle, which is expressed as

$$V = V_s\left(\frac{R(1+G\epsilon_u)}{2R + RG(\epsilon_l + \epsilon_u)} - \frac{1}{2}\right) \approx V_s \frac{G}{4}(\epsilon_u - \epsilon_l) \approx V_s f(\theta) \quad (5)$$

where $f(\theta)$ indicates a function of the bending angle θ, V_s is the bridge supply voltage, V is the bridge output voltage, G is the gauge factor of the strain gauges, R is the resistance of the undeformed sensors, and ϵ_u and ϵ_l indicate the strain of the upper and lower gauge, respectively.

Nylon screen-printing meshes, with thicknesses on the order of 100 μm, were selected as substrates for the layered structure [46]. The substrate material was subjected to tensile testing using a laboratory test bench (F305-EME, Mark-10, US) to assess its elastic modulus and an elastic modulus of 621 MPa was determined from the linear fitting of the stress–strain experimental data.

The simulation environment was exploited to estimate the strain of the joint embedding the layered structure encompassing the selected substrate and to evaluate the reduction of the joint stretch.

The simulated layered structure is shown in Fig. 7, where the substrate is modeled by a nylon mesh embedded in the joint silicone material, whereas the strain gauges were modeled using phenolic resin layers fixed to the nylon mesh. These layers measure 7.4 mm in length (L_ε) and 4.4 mm in width (b_ε), which represent typical dimensions of commercial strain gauges. Their thickness is set at 0.1 mm and includes the adhesive layer used to attach the strain gauges to the substrate. Therefore, the distance between the gauge grids ($h_{2\varepsilon}$) was 0.3 mm.

Fig. 8 highlights the elastic strain distribution within the joint, emphasizing the effects of the embedded layered structure. As noticeable, the strain magnitude near the middle surface is significantly reduced compared to the other regions of the joint. Additionally, the overall strain values are substantially reduced when compared to those shown in Fig. 5. To evaluate the elongation experienced by the sensors, simulation results were exploited to determine the lengths of the lines parallel to the joint axis on the surfaces of the mesh in the deformed state at maximum bending.

Table I reports the obtained results, comparing them to the elongation of lines at the same positions within a joint made of bare silicone, which lacks the layered structure previously described. The curve lengths [for a joint length of 17 mm and sensors placed at the center of the joint as in Fig. 9(a)] are calculated considering the maximum bending angle achieved under the maximum load. In Table I, the strains ϵ'_u (i.e., the

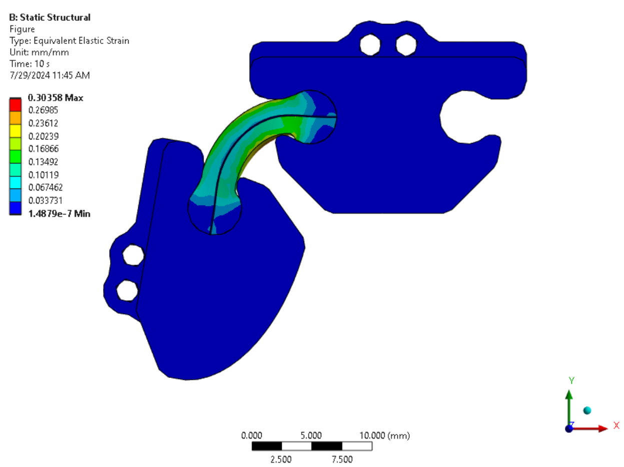

Fig. 8. Equivalent elastic strain distribution in the silicone joint with embedded mesh and mounted strain gauges as in Fig. 9(a).

TABLE I
SIMULATED ELONGATIONS AND STRAIN IN THE BARE SILICONE JOINT AND THE JOINT EMBEDDING THE SENSING STRUCTURE

Case	Distance from the middle surface D (mm)	Upper line length (mm)	Lower line length (mm)	Upper surface strain ϵ'_u (%)	Lower surface strain ϵ'_l (%)	Differential train $\epsilon'_u - \epsilon'_l$ (%)
Silicone	0.05	17.82	17.38	4.85	2.22	2.63
Silicone + mesh	0.05	17.32	16.90	1.88	-0.61	2.49

average strain related to the upper elongated surface) and the strain ϵ'_l (i.e., the average strain of the lower compressed surface) are reported. Additionally, the differential strain ($\epsilon'_u - \epsilon'_l$) is detailed.

For the joint composed of bare silicone, the resulting differential strain due to bending is 2.63% for an undeformed length of 17.0 mm. However, the elongation of both the upper and lower lines reaches 4.85%, which is caused not only by bending but also by the concurrent stretching. On the other hand, when considering the joint with the embedded sensing structure, the simulation results (Table II, row B) show that the maximum overall elongation is reduced to 1.88%, while the differential strain decreases to 2.49%. Hence, the sensitivity of the measurement is almost constant, and with the embedding of the layered structure, the measurement full scale becomes compatible with the target sensing strategy.

A. Strain Gauge Sensor Positioning

A detailed simulation study was also conducted to determine the optimal sensor positioning on the substrate, focusing on the differential strain.

Two additional sensors positions were considered with respect to the one described in Section IV, as visually reported in Fig. 9(b) and (c), all of which allow for the use of the strain gauges in half-bridge configuration. Simulations were performed to obtain strain values on the surfaces of the strain gauges considering the gauge grid position and grid length of 3.2 mm, with an applied force on the moving rigid part of 1.4 N.

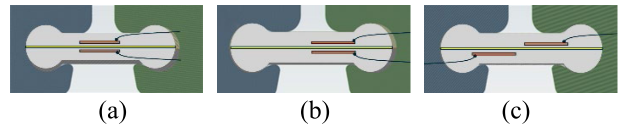

Fig. 9. Strain gauges positioning in different considered scenarios (the drawing is not in scale). (a) Sensors paired in the middle of the joint; (b) sensors paired at one end; and (c) sensors shifted and positioned at the ends.

TABLE II
STRAIN EVALUATION IN THE FOUR SCENARIOS, 1.4-N APPLIED FORCE

Type	upper gauge Strain (%)	lower gauge Strain (%)	Differential Strain (%)	Bending Angle (°)
A	2.50	-1.51	4.01	79.9
B	1.42	-0.45	1.87	79.5
C	1.46	-0.49	1.95	79.5

Table II presents the simulation results in terms of strains for the considered scenarios. It can be observed that the highest differential strain (i.e., the greatest sensing structure response) is obtained with the configuration shown in Fig. 9(a) (SJ A). However, the strain on the upper sensor in this configuration exceeds the sensor full range. The other two configurations produce differential strains that are approximately halved and strains within the full range sensor.

B. Prototyping

Nylon screen meshes (SMs) with different fiber densities were tested as substrates for the strain gauges. Two encapsulated strain gauges were glued to the top and bottom surfaces of the SM at the positions described in Fig. 9.

The used strain gauges (BF350-3AA) feature constantan alloy grids on modified phenolic resin backings, with a nominal resistance of 350 Ω, temperature and creep compensation, a grid size of 3.2 × 3.1 mm, and a backing size of 7.4 × 4.4 mm. The full-scale strain for these sensors is 2.0%. A casting mold was designed to optimally position the SM, allowing for the integration of various substrate geometries [46].

The three considered sensor arrangements (sensor-equipped joints SJ A, SJ B, and SJ C) are expected to exhibit varying mechanical stability and durability of their electrical connections. In particular, referring to the sensor positioning reported in Section III-A, case SJ A involves mounting the sensors in the central part of the joint, placing the gauge connections at the points of greatest flexion. In the other two cases reported (SJ B and C), the connections are protected at the ends of the joint and therefore not subject to flexion during movement.

In sensor prototyping, the choice adhesive for mounting the strain gauge sensors onto the substrate is critical due to the significant bending involved in strain measurement for this application; the mechanical behavior of the adhesive directly influences sensor response, affecting sensitivity, accuracy, fragility, and durability, also potentially inducing creep. For this reason, various types of adhesive compounds were tested.

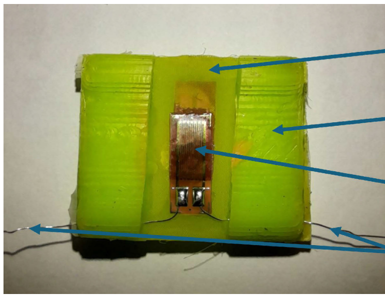

Fig. 10. SJ prototype cutaway.

Two types of adhesives were found to produce reliable and robust sensors: neoprene and cyanoacrylate. Neoprene adhesive was selected for its high shear resistance. However, as an elastomeric adhesive, it is susceptible to the Mullins effect [47], [48]. In contrast, cyanoacrylate adhesive, which is based on ethyl cyanoacrylate monomer, undergoes rapid chain-growth polymerization in the presence of moisture (especially hydroxide ions), forming strong bonds between surfaces without exhibiting the Mullins effect. However, cyanoacrylate adhesive has lower shear strength compared to neoprene-based adhesives. Results from [46] show that sensors using neoprene exhibit good sensitivity and high signal-to-noise ratio, but they suffer from "creep" error, limiting accuracy to about 3°. Therefore, the characterization results reported in this article focus on sensors using cyanoacrylate adhesive.

Different joints have been realized and exploited for experimental validation. In particular, referring to Fig. 9, at least two joints per different strain gauge positioning were realized.

In Fig. 10, we report a cutaway view of an SJ B sample. The strain gauge mounting on the nylon mesh and the electrical connection can be observed, with wires emerging from the sides of the joint, near the support section, where the joint is mounted to the rigid parts. This configuration allows for a stable electrical connection between the strain gauges and the conditioning electronics.

V. Experimental Validation

The validation of the SJ prototypes was conducted using an in-house designed automated test bench, which performed both the calibration of the SJs and durability tests. This test bench is depicted in Fig. 11.

More specifically, the test bench is designed to accommodate the same assembly used in the simulations: a joint connecting two rigid parts fabricated using a 3-D printer. The fixed rigid part is attached to a supporting structure, while the moving part is actuated by a stepper motor through a tendon-based mechanism using a nylon tendon.

To measure the tension in the tendon and, consequently, the force exerted on the moving part, a precision force sensor (Schunk FTN-Nano-17) was connected in series with the tendon. The force sensor was used to verify that the force exerted by the single SJ was in line with the specifications of the drive system used and to interrupt the durability tests in the event of a malfunction in the optical sensors used as limit switches for the joint movements.

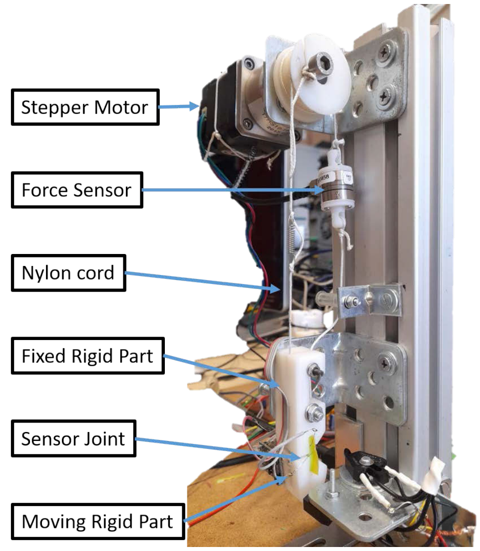

Fig. 11. Test bench, mechanical realization.

The stepper motor is controlled by a microstepping driver. Two photoelectric proximity sensors are used to limit the bending of the structure within a fixed angle range, preventing excessive mechanical load on both the fixed rigid part and the cord. The moving rigid part embeds an accelerometer (ADXL335B, Analog Device, USA) used to evaluate the "reference bending angle" between the fixed rigid part (vertical) and the moving one. Signals coming from the reference accelerometer are acquired by exploiting a data acquisition board (DAQ) (NI USB-6251) having a 16 bits analog to digital converter (ADC) with adjustable input range up to 10 V. As shown in Fig. 12(b), the output from the sensing structure, generated by the resistive bridge composed of two strain gauges and powered by an adjustable reference voltage, is amplified using an analog front end (AFE). The AFE consists of an instrumentation amplifier followed by a gain stage to produce a suitable signal for the ADC embedded in the DAQ and a low-pass filter. Specifically, the dynamics of the conditioning electronics are adjusted to ensure a maximum output signal of 10 V when the strain gauges in the bridge are at full strain. A LabVIEW-based software application was developed to acquire data from the DAQ, the force sensor, and to communicate with the stepper motor driver.

In Fig. 12, the block diagram of the realized measurement test bench is reported. This setup enables the acquisition of signals from the SJs and correlates their responses with the reference bending angle measurements obtained from MEMS accelerometers. The arrangement allows for fully automated tests, controlling the movement of the joint at a consistent speed, which can be adjusted based on the specific test. This enables both sensor calibration and durability testing at various cycle speeds.

A. Calibration Procedure

The realized SJs, which have different strain gauge positions according to Fig. 9 (SJ A, SJ B, and SJ C), were calibrated to obtain the bending angle from the AFE voltage output. The calibration was performed using the reference bending

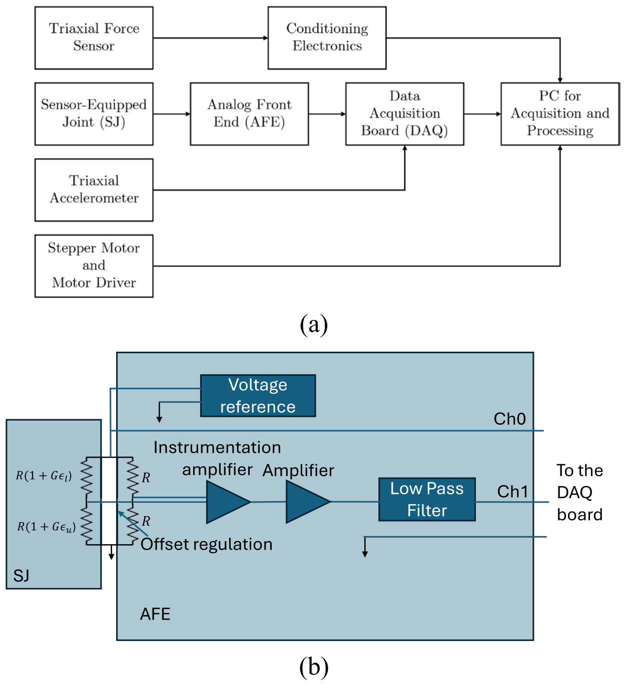

Fig. 12. (a) Block diagram of the test bench for signal acquisition and processing, adopted both for calibrations and durability testing. (b) Block diagram of the AFE.

angle measured by the accelerometer as the ground truth and cyclically moving the rigid part from the rest position (perpendicular to the plane) to a maximum bending angle of 65° and then back to the rest position. The calibration process involved 100 cycles, with each cycle defined as moving from the rest position to the maximum bending angle and back. The calibration speed, defined as the rate of change in bending angle over time, was set to 30°/s.

Only data corresponding to reference bending angles greater than 30° were used for calibration to ensure sufficient accuracy of the reference angle (resulting in 1.2°). A first-order polynomial function was used to fit the AFE output voltage with the measured reference angle

$$\theta_j\left(V_{m,j}\right) = p_{1,j} V_{m,j} + p_{2,j}. \tag{6}$$

Equation (6) shows the fitting function adopted, where $V_{m,j}$ represents the AFE output voltage for the jth SJ and θ_j the measured reference angle estimated with the accelerometer.

The performance of the other SJs (A–C) is very similar in terms of linearity, hysteresis, and overall accuracy.

As an example, Fig. 13 shows the calibration curve for a prototype SJ fabricated, as reported in Fig. 9(b). The blue dots represent the measured data. The AFE voltage output is well represented by a linear relationship with the bending angle over the entire range, and the discrepancy for small angles is due to the loss of accuracy of the reference angle.

Analyzing the results, we observed that the SJs present a little hysteresis introducing errors lower than 1.5°. In Fig. 14(a), the comparison between the angle measured by a calibrated SJ B and the reference angle is reported. As can be noted in the lower subplot, the absolute error between the two is minimal, remaining below 2.5° in the entire range and below

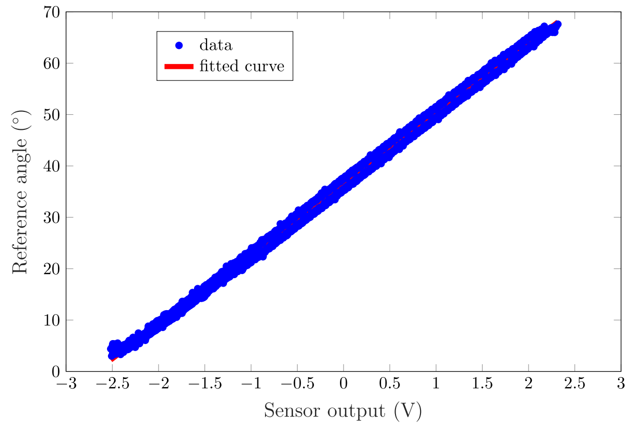

Fig. 13. Calibration curve and experimental data for prototype SJ realized as per Fig. 12(b).

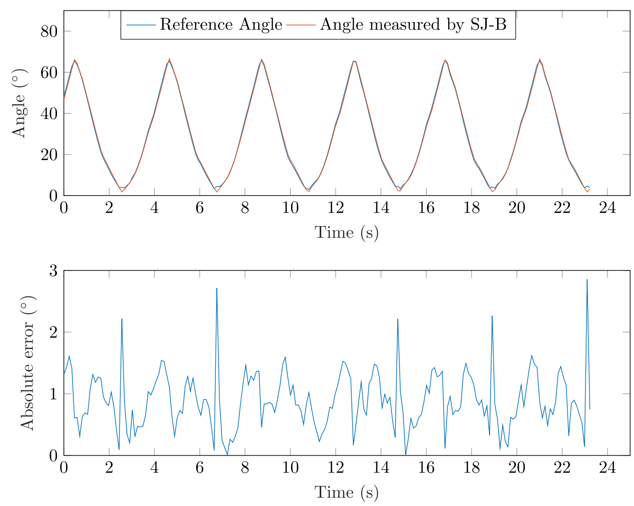

Fig. 14. Comparison between the angle measured by the SJ B and the reference angle, after calibration (upper). Absolute error between the measured and the reference (lower).

TABLE III
SJs Performance Comparison After Calibration

Type	Maximum Error (°)	Root mean squared error (°)
A	4.89	1.73
B	2.83	1.00
C	2.52	1.08

1.5° for angles greater than 30°. Table III shows the errors obtained by comparing the measured angle to the reference angle after calibration for all SJ types over 100 bending cycles. The overall performance is satisfactory, with RMSE values below 2° for all configurations.

The calibration coefficients are consistent with the expected values from the simulations. SJ A has approximately double the sensitivity compared to the others, whereas the other SJ types have similar sensitivity. The joint SJ C has a sensitivity 38.3 mV/° (with V_s = 5 V and an AFE gain of 160).

In Table IV, we report the sensitivities for the three tested SJ types together with the calibration coefficients for (6).

TABLE IV
SJs SENSITIVITY AND CALIBRATION COEFFICIENTS

Type	Sensitivity (mV/°)	Coefficient $p_{1,j}$ (°/V)	Coefficient $p_{2,j}$ (°)
A	82.3	12.2	35.4
B	35.2	28.4	36.7
C	38.3	26.1	37.8

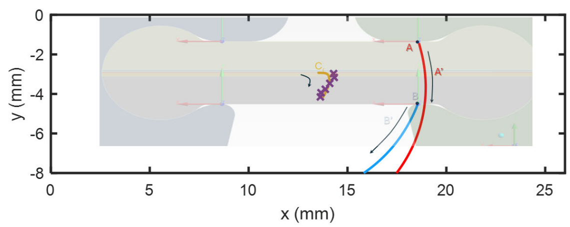

Fig. 15. Orange plot shows the simulated trajectory of the rotation center; the red and the blue curves are the trajectory of points A and B, i.e., the end points of the considered joint section (segment AB). A′ and B′ indicate the same points in the deformed joint during bending. The cross markers are the experimentally located rotation centers of the same section (AB) for six different bending angles (ranging from 38° to 90°).

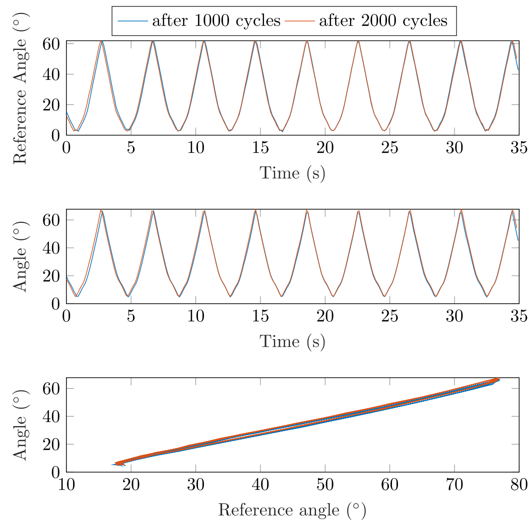

Fig. 16. Results of the durability tests for SJ B. Reference angle as a function of time (upper plot). Bending angles measured by a calibrated SJ B as a function of time (middle plot). Angles measured by SJ B versus reference angles (lower plot).

Besides characterizing the bending angle measurement performance, a study concerning how the positions of the centers of rotation change during bending was conducted. Specifically, the center of rotation of the joint section near the end inserted into the movable rigid part was identified (see segments A and B in Fig. 15) [49] along with the center of rotation of the movable rigid part.

To evaluate how the centers of rotation move during bending, simulations were used, and the obtained results were compared with experimental data obtained from analyzing the photographs of the real joint on the test bench during bending.

The center of rotation of a section of the joint close to the joint end (section AB in Fig. 15) moves from the middle point of the joint along a curved path. For a constant curvature flexible joint, the motion would follow a straight line [49], away from the center, approximately following the trajectory of the middle point during bending.

However, for the considered bending angles, the center moves less than 1 mm along the y-axis and 0.5 mm along the x-axis, so it can be approximately considered fixed during bending, as depicted in Fig. 15.

On the other hand, the rotation center of the rigid movable part follows a similar trajectory, but slightly larger, enclosed in a box of approximately 1 mm per side.

The experimental data confirm the simulations results, as shown in Fig. 15, where the experimentally determined centers for six different bending angles are marked and superimposed on the simulated ones.

B. Durability Test

Each type of joint was tested for reliability. Specifically, at least two specimens of each type were fabricated and tested at a constant speed. The tests were conducted with a maximum bending angle exceeding 65° and a speed of 50°/s. The speed was increased compared to normal operating conditions to subject the joints to higher stress.

Each joint was calibrated according to the procedure described in Section IV-A, and durability was evaluated by monitoring the drift in the measured angle over multiple cycles. As expected, although the performance of SJ A was very good in terms of sensitivity and stability over short periods, its durability proved unsatisfactory due to mechanical stress on the electrical contacts. The average lifespan was a few hundred cycles, after which failures occurred.

The other SJ configurations demonstrated durability, with a lifecycle beyond 3500 cycles, and no critical failures occurred during the tests. An example of the measurement results obtained during the durability tests, which are very similar for SJ B and SJ C, is shown in Fig. 16. This figure illustrates the reference angle from the IMU (upper plots), the angle measured using a calibrated SJ B (middle plots) as functions of time, and the angle assessed by the SJ B as a function of the reference angle. The blue lines represent data collected after 1000 repeated cycles, while the red lines indicate data acquired after 2000 cycles. It can be seen that the SJ behaves stably and that the differences between data windows acquired after 1000 cycles and after 2000 cycles differ less than 1°.

To quantitatively assess operational stability, the maximum and minimum angles reached in each cycle were measured. An example of this stability analysis is shown in Fig. 16 for two SJ B prototypes (one mounted close to the end of the joint supported by the fixed rigid part and the other at the opposite side) and for one SJ C.

In Fig. 17, the outcomes of the durability test are reported. The solid lines represent the maximum angle, and the dashed lines represent the minimum angle (upper plots) as a function of the test cycle number during the durability tests and their drifts (lower plots), i.e., the deviations with respect to their initial values. The drift experienced by both SJs is similar, remaining below 2° over the course of 3500 cycles (as shown

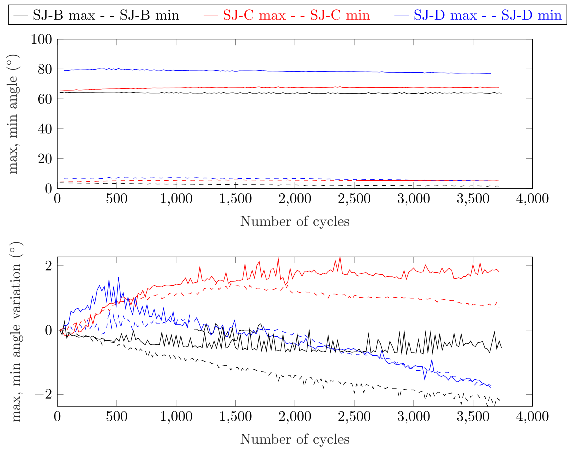

Fig. 17. Results of the durability tests for SJ B1 at the fixed end (blue lines), SJ B2 at the moving end (red lines), and SJ C (black lines). Solid lines indicate the maximum angle reached at each repeated test cycle as a function of the test cycle number. Dashed lines show the minimum angle reached in each repeated test cycle as a function of the test cycle number (upper plot). Drift observed during the cycling process, represented by the deviation of the maximum (solid lines) and minimum angles (dashed lines) from their initial values (lower plot). The reported experiments lasted at least 4 h of continuous cycling.

more clearly in the lower panel of Fig. 17). Notably, the most significant variations occurred in the early stages of the test, with the drift gradually decreasing as the test progressed, suggesting that the mechanical assembly reaches a stable state after extended use.

The SJ configurations proposed in Fig. 9(b) and (c), which allow for a half-bridge configuration and minimize the mechanical stress on the electrical contacts, provided satisfactory durability and reliability. The gradual reduction in drift indicates that prolonged usage helps stabilize the sensor-equipped joints, potentially improving their long-term performance. This suggests that after an initial break-in period, the mechanical and electrical interfaces become more stable, further enhancing joint performance during prolonged operations.

VI. Conclusion

This study investigated the operational stability and calibration of sensor-equipped joints under varying conditions. The proposed solution of embedding a layered structure with metal thin-film or foil strain gauges in half bridge configuration effectively solves the problem of measuring bending angles in robots embedding soft joints. The classical half-bridge configuration utilized in this work provided accurate bending measurements while reducing the influence of residual stretching, compression, and torsion.

The proposed sensing solution provides linear output and allows for accuracy better than 2°. The analysis showed that sensor performance remains stable with drifts staying below 2° throughout 3500 cycles. Notably, significant variations were primarily observed in the early stages of testing, with subsequent cycles revealing diminishing drift, thereby demonstrating the suitability of these sensors in practical applications.

The SJ configurations B and C showed similar performance in terms of sensitivity and, while the configuration with overlapping strain gauges is preferable because it ensures better common-mode noise rejection, the alternative configuration, which distributes the strain gauges across the two ends of the joint, may offer advantages in terms of contact distribution and potentially more efficient wiring. Each setup presents tradeoffs, with the choice depending on the priority given to noise rejection versus wiring simplicity.

Overall, the findings suggest that the developed SJ configurations are durable and reliable, with prolonged usage leading to improved stability and performance. These results underline the potential for embedding sensor-equipped joints in various applications, paving the way for future research to further enhance soft robot proprioceptive capability.

TABLE V

Details of Materials and Instrumentation

Item	Specifications
Silicone	Silicone R-PRO Fast (Reschimica, IT), about 5 grams for each joint
3D printer	In the proposed work we used a Formlabs v4 (Formlabs, US). Any 3D printer with comparable performance is fine
Strain Gauges	BF350-3AA (Youmile, RPC). Resistance: 349.8+/-0.1 ohm Sensitivity Coefficient: 2.0-2.20
Conditioning Electronics	GW Instek GPS-4303 200W (Good Will Instrument Co., TW), followed by a voltage reference and equipped with an instrumentation amplifier followed by gain stages (based on instrumentation amplifier INA128 and OP177 amplifier)
Acquisition Board	DAQ NI USB-6251 (National Instruments, US)
Stepper Motor	Nema 17HS19-1684S (StepperOnline, US)
Stepper Motor Driver	DM320T Stepper Motor digital driver (StepperOnline, US)

Appendix

In Table V, we detail the materials alongside the specifications of the materials and instruments used to fabricate and test the proposed sensorized joints.

Acknowledgment

The authors would like to thank Leonardo Franco for his assistance in developing and preparing the joint, as well as for providing essential advice in preparing the silicone casting mold.

References

[1] P. Ferrentino, S. K. Tabrizian, J. Brancart, G. V. Assche, B. Vanderborght, and S. Terryn, "FEA-based inverse kinematic control: Hyperelastic material characterization of self-healing soft robots," *IEEE Robot. Autom. Mag.*, vol. 29, no. 3, pp. 78–88, Sep. 2022.

[2] H. B. Khaniki, M. H. Ghayesh, R. Chin, and M. Amabili, "Hyperelastic structures: A review on the mechanics and biomechanics," *Int. J. Non-Linear Mech.*, vol. 148, Jan. 2023, Art. no. 104275.

[3] N. Gariya, P. Kumar, and B. Prasad, "Stress and bending analysis of a soft pneumatic actuator considering different hyperelastic materials," *Mater. Today, Proc.*, vol. 65, pp. 3126–3131, Jan. 2022.

[4] B. J. Caasenbrood, A. Y. Pogromsky, and H. Nijmeijer, "Dynamic modeling of hyper-elastic soft robots using spatial curves," *IFAC-PapersOnLine*, vol. 53, no. 2, pp. 9238–9243, 2020.

[5] C. Lee et al., "Soft robot review," *Int. J. Control, Autom. Syst.*, vol. 15, no. 1, pp. 3–15, Feb. 2017.

[6] A. J. Veale, I. A. Anderson, and S. Q. Xie, "The smart peano fluidic muscle: A low profile flexible orthosis actuator that feels pain," *Proc. SPIE*, vol. 9435, Mar. 2015, Art. no. 94351V.

[7] S. Cheng, Y. S. Narang, C. Yang, Z. Suo, and R. D. Howe, "Stick-on large-strain sensors for soft robots," *Adv. Mater. Interface*, vol. 6, no. 20, Oct. 2019, Art. no. 1900985.

[8] W. Dong, K. Sheng, B. Huang, K. Xiong, K. Liu, and X. Cheng, "Stretchable self-powered TENG sensor array for human-robot interaction based on conductive ionic gels and LSTM neural network," *IEEE Sensors J.*, vol. 24, no. 22, pp. 37962–37969, Nov. 2024, doi: 10.1109/JSEN.2024.3464633.

[9] H. Souri et al., "Wearable and stretchable strain sensors: Materials, sensing mechanisms, and applications," *Adv. Intell. Syst.*, vol. 2, no. 8, Aug. 2020, Art. no. 2000039.

[10] J.-S. Noh, "Conductive elastomers for stretchable electronics, sensors and energy harvesters," *Polymers*, vol. 8, no. 4, p. 123, Apr. 2016.

[11] E. L. White, J. C. Case, and R. K. Kramer, "Multi-element strain gauge modules for soft sensory skins," *IEEE Sensors J.*, vol. 16, no. 8, pp. 2607–2616, Apr. 2016.

[12] T. Yorozu, M. Hirano, K. Oka, and Y. Tagawa, "Electron spectroscopy studies on magneto-optical media and plastic substrate interface," *IEEE Transl. J. Magn. Jpn.*, vol. JMJ-2, no. 8, pp. 740–741, Aug. 1987.

[13] P. Roberts, M. Zadan, and C. Majidi, "Soft tactile sensing skins for robotics," *Current Robot. Rep.*, vol. 2, no. 3, pp. 343–354, Jul. 2021.

[14] O. Atassi, "Design of a robotic finger for grasping enhancement," M.S. thesis, Dept. Inf. Eng. Math., Univ. Siena, Siena, Italy, 2011.

[15] D. Prattichizzo, M. Malvezzi, I. Hussain, and G. Salvietti, "The sixth-finger: A modular extra-finger to enhance human hand capabilities," in *Proc. 23rd IEEE Int. Symp. Robot Hum. Interact. Commun.*, Aug. 2014, pp. 993–998.

[16] R. Ma and A. Dollar, "Yale OpenHand project: Optimizing open-source hand designs for ease of fabrication and adoption," *IEEE Robot. Autom. Mag.*, vol. 24, no. 1, pp. 32–40, Mar. 2017.

[17] S. Kim, C. Laschi, and B. Trimmer, "Soft robotics: A bioinspired evolution in robotics," *Trends Biotechnol.*, vol. 31, no. 5, pp. 287–294, May 2013.

[18] R. Deimel and O. Brock, "A compliant hand based on a novel pneumatic actuator," in *Proc. IEEE Int. Conf. Robot. Autom.*, May 2013, pp. 2047–2053.

[19] P. Polygerinos et al., "Soft robotics: Review of soft actuators and sensors," *Adv. Mater.*, vol. 29, no. 27, 2017, Art. no. 1604977.

[20] D. Prattichizzo et al., "Human augmentation by wearable supernumerary robotic limbs: Review and perspectives," *Prog. Biomed. Eng.*, vol. 3, no. 4, Oct. 2021, Art. no. 042005.

[21] E. Turco, V. Bo, M. Pozzi, A. Rizzo, and D. Prattichizzo, "Grasp planning with a soft reconfigurable gripper exploiting embedded and environmental constraints," *IEEE Robot. Autom. Lett.*, vol. 6, no. 3, pp. 5215–5222, Jul. 2021, doi: 10.1109/LRA.2021.3072855.

[22] R. R. Ma, L. U. Odhner, and A. M. Dollar, "A modular, open-source 3D printed underactuated hand," in *Proc. IEEE Int. Conf. Robot. Autom.*, May 2013, pp. 2737–2743, doi: 10.1109/ICRA.2013.6630954.

[23] M. Totaro, A. Mondini, A. Bellacicca, P. Milani, and L. Beccai, "Integrated simultaneous detection of tactile and bending cues for soft robotics," *Soft Robot.*, vol. 4, no. 4, pp. 400–410, Dec. 2017.

[24] M. Su et al., "Pneumatic soft actuator with anisotropic soft and rigid restraints for pure in-plane bending motion," *Appl. Sci.*, vol. 9, no. 15, p. 2999, Jul. 2019.

[25] C. Majidi, R. Kramer, and R. J. Wood, "A non-differential elastomer curvature sensor for softer-than-skin electronics," *Smart Mater. Struct.*, vol. 20, no. 10, Oct. 2011, Art. no. 105017.

[26] J.-B. Chossat, Y.-L. Park, R. J. Wood, and V. Duchaine, "A soft strain sensor based on ionic and metal liquids," *IEEE Sensors J.*, vol. 13, no. 9, pp. 3405–3414, Sep. 2013.

[27] R. K. Kramer, C. Majidi, R. Sahai, and R. J. Wood, "Soft curvature sensors for joint angle proprioception," in *Proc. IEEE/RSJ Int. Conf. Intell. Robots Syst.*, Sep. 2011, pp. 1919–1926.

[28] S. Russo, T. Ranzani, H. Liu, S. Nefti-Meziani, K. Althoefer, and A. Menciassi, "Soft and stretchable sensor using biocompatible electrodes and liquid for medical applications," *Soft Robot.*, vol. 2, no. 4, pp. 146–154, Dec. 2015.

[29] S. Sareh, Y. Noh, M. Li, T. Ranzani, H. Liu, and K. Althoefer, "Macrobend optical sensing for pose measurement in soft robot arms," *Smart Mater. Struct.*, vol. 24, no. 12, Dec. 2015, Art. no. 125024.

[30] E. Fujiwara and T. D. Cabral, "Optical fiber specklegram sensor for multi-point curvature measurements," *Appl. Opt.*, vol. 61, no. 23, p. 6787, Aug. 2022.

[31] S. Ozel, N. A. Keskin, D. Khea, and C. D. Onal, "A precise embedded curvature sensor module for soft-bodied robots," *Sens. Actuators A, Phys.*, vol. 236, pp. 349–356, Dec. 2015.

[32] G. Saggio, F. Riillo, L. Sbernini, and L. R. Quitadamo, "Resistive flex sensors: A survey," *Smart Mater. Struct.*, vol. 25, no. 1, Jan. 2016, Art. no. 013001.

[33] K. Elgeneidy, N. Lohse, and M. Jackson, "Bending angle prediction and control of soft pneumatic actuators with embedded flex sensors—A data-driven approach," *Mechatronics*, vol. 50, pp. 234–247, Apr. 2018.

[34] G. Gerboni, A. Diodato, G. Ciuti, M. Cianchetti, and A. Menciassi, "Feedback control of soft robot actuators via commercial flex bend sensors," *IEEE/ASME Trans. Mechatronics*, vol. 22, no. 4, pp. 1881–1888, Aug. 2017.

[35] B. Kim et al., "A comparison among Neo-Hookean model, Mooney-Rivlin model, and Ogden model for chloroprene rubber," *Int. J. Precis. Eng. Manuf.*, vol. 13, no. 5, pp. 759–764, May 2012.

[36] P. A. L. S. Martins, R. M. Natal Jorge, and A. J. M. Ferreira, "A comparative study of several material models for prediction of hyperelastic properties: Application to silicone-rubber and soft tissues," *Strain*, vol. 42, no. 3, pp. 135–147, Aug. 2006.

[37] S. K. Melly, L. Liu, Y. Liu, and J. Leng, "A review on material models for isotropic hyperelasticity," *Int. J. Mech. Syst. Dyn.*, vol. 1, no. 1, pp. 71–88, Sep. 2021.

[38] A. Schiavi, R. Cuccaro, and A. Troia, "Strain-rate and temperature dependent material properties of agar and gellan gum used in biomedical applications," *J. Mech. Behav. Biomed. Mater.*, vol. 53, pp. 119–130, Jan. 2016.

[39] A. Schiavi and A. Prato, "Evidences of non-linear short-term stress relaxation in polymers," *Polym. Test.*, vol. 59, pp. 220–229, May 2017.

[40] A. Schiavi, R. Cuccaro, and A. Troia, "Functional mechanical attributes of natural and synthetic gel-based scaffolds in tissue engineering: Strain-stiffening effects on apparent elastic modulus and compressive toughness," *J. Mech. Behav. Biomed. Mater.*, vol. 126, Feb. 2022, Art. no. 105066.

[41] M. Jaspers, M. Dennison, M. F. J. Mabesoone, F. C. MacKintosh, A. E. Rowan, and P. H. J. Kouwer, "Ultra-responsive soft matter from strain-stiffening hydrogels," *Nature Commun.*, vol. 5, no. 1, Dec. 2014.

[42] *Rubber, Vulcanized or Thermoplastic—Determination of Hardness Part 4: Indentation Hardness by Durometer Method (Shore Hardness)*, document ISO 48-4, 2018.

[43] J. Kunz and M. Studer, "Determining the modulus of elasticity in compression via Shore-A hardness," *Kunststoffe Int.*, vol. 96, no. 6, pp. 92–94, 2006.

[44] J. H. Wu and Q. Jia, "The heterogeneous energy landscape expression of KWW relaxation," *Sci. Rep.*, vol. 6, no. 1, p. 20506, Feb. 2016.

[45] A. Schiavi and A. Prato, "Non-linear stress relaxation of polymers: Experimental evidences and stretched exponential model," in *Proc. ICSV*, 2016, p. 2.

[46] E. Landi et al., "A method for sensing passive joints of robotic extra fingers for trajectory tracking," in *Proc. IEEE Int. Workshop Metrology Ind. 4.0 IoT (MetroInd4.0&IoT)*, May 2024, pp. 562–567.

[47] D. Allen, *Stiffness Evaluation of Neoprene Bearing Pads Under Long-Term Loads*, vol. 70. FL, USA: University of Florida, Department of Transportation, Research Center, Dept. of Civil and Coastal Engineering, 2008.

[48] L. Zhan, S. Qu, and R. Xiao, "A review on the mullins effect in tough elastomers and gels," *Acta Mechanica Solida Sinica*, vol. 37, no. 2, pp. 181–214, Apr. 2024, doi: 10.1007/s10338-023-00460-6.

[49] M. Verotti, "Analysis of the center of rotation in primitive flexures: Uniform cantilever beams with constant curvature," *Mechanism Mach. Theory*, vol. 97, pp. 29–50, Mar. 2016.

Elia Landi (Member, IEEE) received the M.Sc. degree in electronics and communications engineering and the Ph.D. degree in information engineering from the University of Siena, Siena, Italy, in 2017 and 2021, respectively.

He is currently a Research Associate at the Department of Information Engineering and Mathematics, University of Siena. His current research interests include the design and testing of measurement systems for vibration analysis, design, and development of modular test benches for electromechanical parts durability and testing and study and design of measurement systems related to turbomachine condition monitoring and measurement systems for biomedical applications.

Tommaso Lisini Baldi (Member, IEEE) received the M.Sc. (cum laude) degree in computer and automation engineering and the Ph.D. degree in robotic and automation from the Department of Information Engineering and Mathematics, University of Siena, Siena, Italy, in 2014 and 2018, respectively.

He was a Ph.D. Fellow with the Department of Advanced Robotics, Istituto Italiano di Tecnologia, Genoa, Italy, from 2014 to 2017. Currently, he is an Assistant Professor at the University of Siena, and a Research Affiliate at the Istituto Italiano di Tecnologia. His research interests include robotics and haptics focusing on human–robot collaboration, haptic feedback, wearable technologies, and motion tracking with inertial sensors.

Jonas Papenbrock (Student Member, IEEE) received the B.Sc. degree in mechanical engineering from Czech Technical University in Prague, Prague, Czechia, in 2012, and the M.Sc. degree from the Technical University of Dortmund, Dortmund, Germany, in 2020, specializing in production technology and robotics. He is currently pursuing the Ph.D. degree with the University of Siena, Siena, Italy, focusing on flexible sensors and soft robotic tactile techniques. His thesis work was conducted at RCMT, Prague, and Charité—University Hospital Berlin, Berlin, Germany.

He also participated in a bilateral exchange at the Costa Rica Institute of Technology, Cartago, Costa Rica.

Alessio Facello (Member, IEEE) received the M.Sc. degree in mechatronics engineering from the Polytechnic University of Turin, Turin, Italy, in 2009.

He is a Research Technologist at the Applied Metrology and Engineering Division, National Institute of Metrological Research (INRiM), Turin. During the Research Assistant activity at CNR (National Research Council) got the Ph.D. gaining expertise in design and development of complex multiparameter data acquisition systems in the field of applied mechanics. His main areas of focus are vibrations, gravimetry, and force.

Andrea Prato (Member, IEEE) received the M.Sc. degree in physics from the University of Turin, Turin, Italy, in 2011, and the Ph.D. degree in metrology from the Politecnico di Torino, Turin, in 2015.

He is a Researcher at the Applied Metrology and Engineering Division, National Institute of Metrological Research (INRiM), Turin. He is the Vice Convenor of EURAMET TC-M (Mass and Related Quantities) SC Force and member of IMEKO TC-3 (Measurement of Force and Mass) and TC-5 (Measurement of Hardness). He is also an Adjunct Professor at Politecnico di Torino, Turin. His main metrology and research areas are force, hardness, gravimetry, vibrations, acoustics, and mechanical properties of materials.

Alessandro Schiavi (Member, IEEE) received the M.Sc. degree in physics from the University of Turin, Turin, Italy, in 2002.

He is a Senior Research Scientist at the National Institute of Metrological Research (INRiM), Turin. From 2002 to 2006, he was a Researcher Assistant with the Acoustic Department, National Electrotecnical Institute "Galileo Ferraris," Turin. From 2007 to 2012, he was a Researcher with the Thermodynamics Division, INRiM; since 2012, he has been responsible for vibrations, primary and secondary standard calibration, with the Applied Metrology and Engineering Division, INRiM. He has been an Adjunct Professor in noise control engineering at Politecnico di Torino, Turin, since 2012. His research interests include vibration fundamental metrology, environmental and mechanical vibrations, structural acoustics, mechanical, and physical properties of materials.

Marco Mugnaini (Member, IEEE) received the Laurea degree in electronics engineering with major in nonlinear automatic controls and the Ph.D. degree in reliability availability and logistics from the University of Florence, Florence, Italy, in 1999 and 2003, respectively.

He was a Product Safety Engineer at the General Electric (GE) Power System Oil and Gas Division, University of Florence, from 2003 to 2005, with the responsibility of leading the design for safety. From 2005 to 2012, he was an Assistant Professor at the University of Siena, Siena, Italy. He was appointed as a Faculty and a Professor at the Department of Electrical and Electronics Technology, Higher Colleges of Technology Abu Dhabi, United Arab Emirates, from 2012 to 2013. Currently, he is an Associate Professor at the University of Siena. He has written more than 250 science papers and a book titled *Dependability in a Packet*.

Dr. Mugnaini is the IEEE I&M Distinguished Lecturer from 2017 to 2020.

Domenico Prattichizzo (Fellow, IEEE) received the M.S. degree in electronics engineering and the Ph.D. degree in robotics and automation from the University of Pisa, Pisa, Italy, in 1991 and 1995, respectively.

In 1994, he was a Visiting Scientist with the MIT AI Laboratory, Cambridge, MA, USA. He is a Professor of Robotics with the University of Siena, Siena, Italy, and since 2009, he has been a Scientific Consultant with Istituto Italiano di Tecnologia, Genoa, Italy. He has authored more than 200 papers in his research fields. His main research interests include haptics, grasping, visual servoing, and mobile robotics.

Ada Fort (Member, IEEE) received the Laurea degree in electronic engineering and the Ph.D. degree in nondestructive testing from the University of Florence, Florence, Italy, in 1989 and 1992, respectively.

She is currently a Full Professor at the Department of Information Engineering and Mathematical Sciences, University of Siena, Siena, Italy. Her interests concern the development of measurement systems based on chemical and ultrasonic sensors and the development of automatic fault diagnosis systems. Recently, she has been involved in the study of random number generators based on chaotic maps.